

## THE ASYMMETRIC BOWSHOCK/PWN OF PSR J2124–3358

ROGER W. ROMANI<sup>1</sup>, PATRICK SLANE & ANDREW GREEN

*Submitted to ApJ*

### ABSTRACT

We describe new measurements of the remarkable  $H\alpha$ /UV/X-ray bowshock and pulsar wind nebula of the isolated millisecond pulsar PSR J2124–3358. *CXO* imaging shows a one-sided jet structure with a softer equatorial outflow. KOALA IFU spectroscopy shows that non-radiative emission dominates the bow shock and that the  $H\alpha$  nebula is asymmetric about the pulsar velocity with an elongation into the plane of the sky. We extend analytic models of the contact discontinuity to accommodate such shapes and compare these to the data. Using *HST* UV detections of the pulsar and bow shock, radio timing distance and proper motion measurements and the *CXO*-detected projected spin axis we model the 3-D PWN momentum flux distribution. The integrated momentum flux depends on the ionization of the ambient ISM, but for an expected ambient WNM we infer  $I = 2.4 \times 10^{45} \text{ g cm}^2$ . This implies  $M_{NS} = 1.6 - 2.1 M_{\odot}$ , depending on the equation of state, which in turn suggests that the MSP gained significant mass during recycling and then lost its companion. However, this conclusion is at present tentative, since lower ionization allows  $\sim 30\%$  lower masses and uncertainty in the parallax allows up to 50% error.

*Subject headings:* pulsars: individual: PSR J2124–3358 – shock waves – dense matter

### 1. INTRODUCTION

The standard paradigm for pulsar recycling involves mass and angular momentum accretion in a binary (Bisnovaty-Kogan & Komberg 1974; Smarr & Blandford 1976). Yet a number of recycled pulsars, especially short period millisecond pulsars (MSP) are isolated. An attractive scenario for such single MSP invokes evolution through an extreme ‘Black Widow’ phase where the MSP spindown power completely evaporates a companion (Ruderman, Shaham & Tavani 1989). The critical prediction of this scenario is a heavy neutron star. For an isolated (non-binary) pulsar this would seem impossible to test. However, we have proposed (Brownsberger & Romani 2014, hereafter BR14) that if a sufficiently accurate measurement of the total spindown power  $\dot{E}$  can be made, using detailed measurements of a pulsar bow shock, this can be compared with  $I\Omega\dot{\Omega}$ , yielding the neutron star moment of inertia  $I$ . Since  $I$  increases along with mass, this provides a test of the recycling scenario.

The  $H\alpha$  bow shock of PSR J2124–3358 (hereafter J2124) discovered by Gaensler, Jones & Stappers (2002) provides an opportunity for such a test. This 4.9 ms pulsar is nearby and pulsar timing has provided a high accuracy parallax distance  $d = 0.41_{-0.07}^{+0.09}$  kpc and proper motion  $v_{\perp} = 101.2 \pm 0.8 \text{ km s}^{-1}$  at a position angle of  $195.77 \pm 0.08^{\circ}$  (Reardon et al. 2016). If we correct for the standard solar motion (Johnson & Soderblom 1987) at  $d = 410$  pc the transverse velocity is  $v_{\perp} = 110.1 \pm 0.8 \text{ km s}^{-1}$  at  $202.98 \pm 0.08^{\circ}$ . BR14 made new, deeper  $H\alpha$  images of the nebula, measuring the shape and flux of the apex. An archival December 19, 2004 30 ks *CXO* ACIS observation of the pulsar (ObsID 5585, Chatterjee, PI) revealed, in addition to the pulsar point source, a diffuse X-ray pulsar wind nebula (PWN) within the  $H\alpha$  bowshock with a long jet or trail extending to the NW, following the  $H\alpha$  limb. These data were briefly analyzed by Hui & Becker (2006), who also studied a lower-resolution

*XMM-Newton* exposure. Their analysis showed a soft point source and somewhat harder spectrum for the PWN jet/trail.

Recently Rangelov et al. (2017) have reported on *HST* *SBC/WFC3* observations of the pulsar. These data detect both the pulsar point source and an arc of UV emission (best seen in the F125LP filter) from the bow shock itself. These data are very important in measuring the distance from the pulsar to the shock limb which is  $1.8''$  along the projected pulsar velocity vector. We show below that, within ground-based resolution, this is also the offset to the  $H\alpha$  shock limb. This very small stand-off, and the flat shock near the apex are important constraints on the pulsar wind distribution and integrated momentum flux. In this paper we explore the PWN geometry with new observations and models. These give insights into the pulsar wind structure and spindown energetics. We comment on the implications for the neutron star moment of inertia and the recycling scenario.

### 2. NEW OBSERVATIONS

We describe here new, deeper *CXO* observations probing the PWN spectrum and morphology, an attempt at improved *HST* astrometry and a new AAT/KOALA observation to measure the velocity structure and optical spectrum of the bow shock apex. Together these data give a refined view of the PWN/bow shock structure, and conditions in the surrounding ISM.

#### 2.1. *Chandra* imaging

We obtained new *CXO* ACIS-S imaging of J2214 with two exposures: 93 ks on July 7, 2016 (ObsID 17900) and 85 ks on September 4, 2016 (ObsID 19686) with the source placed near the aimpoint of the S3 chip. All data were useful with no strong background flares. Standard ACIS processing was used to align all exposures to the December 19, 2004 (ObsID 5585) archival frame, checked by matching field sources. The  $0.6''$  proper motion shift over the 11.5 year gap was obvious. The overall spectrum is very soft, with only a few point source counts above 3 keV. This is not unexpected, given the close distance. This distance and the low disper-

<sup>1</sup> Department of Physics, Stanford University, Stanford, CA 94305-4060, USA; rwr@astro.stanford.edu

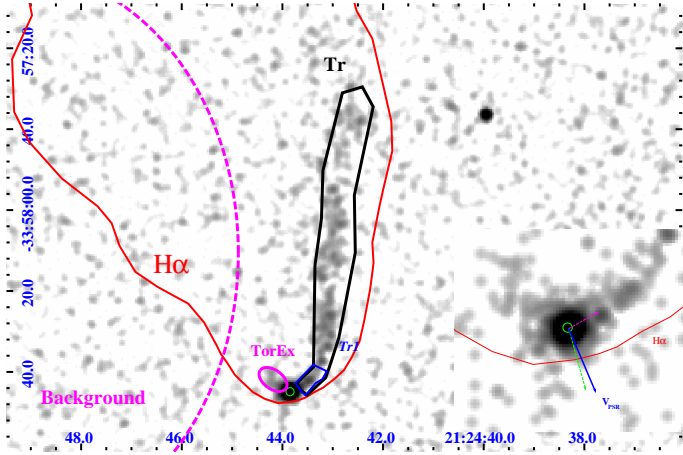


FIG. 1.— Combined 0.3-3 keV CXO image, smoothed with a  $\sigma = 1.5''$  Gaussian. The limb of the  $H\alpha$  bow shock encloses the trailed reverse shock X-ray PWN. Some spectral extraction regions are indicated. The  $20''$  inset shows the region around the pulsar smoothed at  $0.75''$ , with the  $H\alpha$  limb location for reference. The proper motion vector (green dashed arrow) and the motion corrected to the local standard of rest (blue arrow) are both plotted with a length showing the displacement over 100 y. The initial trail (polar outflow) axis is shown in magenta. An equatorial extension to the PSF is visible near the initial axis.  $1.6\text{ cm}^{-3}\text{ pc}$  imply an absorption column  $N_H \approx 1 - 3 \times 10^{20}\text{ cm}^{-2}$  (Rangelov et al. 2017). With such low absorption and a relatively soft source, the progressive ACIS contamination and low energy effective area loss are particularly severe. However, with the longer 2016 exposures, we do accrue somewhat larger image counts than in the archival observation.

We re-aligned the data, referencing to the point source (2004.97 epoch) and merged the exposures. The improved statistics provide a better view of fine structure near the pulsar. The strongest feature is the extension that leaves the pulsar at  $PA = -60^\circ$ , and then sweeps north to stay within the  $H\alpha$  limb. This is most prominent at intermediate  $\sim 1.5 - 3$  keV energies. We will refer to this as the ‘Trail’ although as argued below, its morphology and relatively hard spectrum suggest identification as a pulsar polar jet. At lower  $< 1.5$  keV energy, an elliptical extension to the point source is apparent, with major axis radius  $\sim 3''$  transverse to the jet. We identify this softer emission with an equatorial outflow describable as a ‘torus’ in many PWNe. To the NE ( $PA \approx 45^\circ$ ) this emission persists for another  $\sim 4''$ . This can be interpreted as the sweep back of the equatorial outflow, as it reverse shocks inside the  $H\alpha$  forward shock envelope. Although there are a handful of X-ray counts along the axis opposite the jet, such a ‘forward’ jet is not well detected. Similarly the equatorial outflow appears to be terminated to the SW, where it reaches the forward shock.

We have made some basic spectral measurements of these X-ray structures. Using the regions defined in figure 1, we extracted counts from the aligned exposures and fit to thermal and power law models, with Galactic absorption using the Wilms, Allen & McCray (2000) *xstbabs* model. Background was extracted from a nearby source-free region on the S3 chip.

For the pulsar-dominated point source (PS, 2020 background-subtracted counts) we used a  $1''$  radius aperture to minimize contamination from the surrounding diffuse emission. Pile-up is negligible. A pure thermal fit indicates a low absorption, but high energy excess makes it statistically

TABLE 1  
ACIS SPECTRAL FITS

Reg.	$N_H$ b	$\Gamma$	$f_{PL}$ c	kT keV	$R_{BB}$ km	P(Q)
PS	$0.03^{+0.5}_{-0.03}$			$0.27^{+0.03}_{-0.02}$	0.059	$10^{-5}$
PS	$20^{+5}_{-3}$	$3.64^{+0.15}_{-0.14}$	$47^{+5}_{-4}$			0.72
PS <sup>d</sup>	$0^{+9}_{-0}$	$2.6^{+0.4}_{-2.3}$	0.039	$0.25^{+0.01}_{-0.06}$	0.078	0.03
PS	$0^{+2}_{-0}$	$2.5^{+0.2}_{-0.1}$	$7^{+1}_{-1}$	$0.25^{+0.01}_{-0.01}$	0.047	0.96
Tr	$0^{+5}_{-0}$	$2.15^{+0.23}_{-0.14}$	$1.8^{+0.2}_{-0.2}$			0.81
Tr	$1^a$	$2.19^{+0.15}_{-0.15}$	$1.9^{+0.2}_{-0.2}$			0.84
TorEx	$1^a$	$3.66^{+0.7}_{-0.6}$	$0.2^{+0.07}_{-0.07}$			0.72
Tr1	$1^a$	$2.46^{+0.5}_{-0.5}$	$0.3^{+0.05}_{-0.05}$			0.49
Tr2	$1^a$	$2.10^{+0.16}_{-0.15}$	$1.6^{+0.1}_{-0.1}$			0.66

All errors are projected  $1\sigma$  values. P(Q) gives the probability of the fit  $\chi^2$ .

<sup>a</sup>  $N_H$  fixed at  $10^{20}\text{ cm}^{-2}$ .

<sup>b</sup> Wilms model absorption in  $10^{20}\text{ cm}^{-2}$

<sup>c</sup> Unabsorbed 0.3-7keV flux in  $10^{-14}\text{ erg cm}^{-2}\text{ s}^{-1}$ .

<sup>d</sup> Double BB fit. ‘PL’ parameters are  $kT$  and  $R_{BB}$  for the hot blackbody component.

unacceptable. A pure powerlaw fit is statistically adequate, but requires an unrealistically high absorption to accommodate the low energy spectral peak. Thus a two component model is required. If two blackbodies are used the covariance is large and the parameters poorly determined. The fit leaves residuals at high energy, leading to a low fit probability P(Q). A powerlaw plus blackbody fit is fully adequate, with about half the counts from each component. The absorption is not well determined with an upper limit of  $2 \times 10^{20}\text{ cm}^{-2}$ . The thermal component has a high temperature  $2.9 \times 10^6\text{ K}$  and a small effective area (spherical radius 47 m, 2-D cap radius 94 m at 410 pc) indicating emission from a heated polar cap. We lack the sensitivity to meaningfully fit for a neutron star atmosphere model, but as seen in the XMM fits of Zavlin (2006), a light element atmosphere would decrease the cap temperature by  $\sim 2\times$  and increase the cap radius by  $\sim 4\times$ . Zavlin (2006) also finds a pulse fraction of  $56 \pm 14\%$  in the XMM data (which includes the extended emission). This indicates that the pulse fraction of the point source is very high. This pulsar is to be studied in the NICER core program and it is expected that a much more detailed understanding of the pulse spectrum will be available soon. However the NICER steady unpulsed component will include the extended non-thermal emission resolved in these ACIS data.

For the diffuse components, we first measured the spectrum of the full  $80''$ -length trail (Tr, 545 background-subtracted counts), finding a typical PWN powerlaw index  $\Gamma = 2.15$ . The absorption is only constrained to be  $< 5 \times 10^{20}\text{ cm}^{-2}$ . To spectrally compare diffuse components we adopt a fixed  $N_H = 10^{20}\text{ cm}^{-2}$  (mid point of the BB+PL  $N_H$  range) and fit only for fluxes and power law indices. A check of the  $\sim 8''$  trail before the ‘kink’ where it approaches the  $H\alpha$  limb (Tr1, 64 background-subtracted counts), gave a somewhat softer index (2.5) than the remainder of the trail (Tr2=Tr-Tr1, 481 background-subtracted counts) beyond the kink (2.1). This difference is not statistically significant, but we certainly do not detect synchrotron aging along the trail. Interestingly the ‘torus’ extension to the NE (TorEx, 42 background-subtracted counts) is substantially softer than the trail (at  $\Gamma \approx 3.7$ ). The general diffuse emission around the point source seems similarly soft, and this may bias the ‘pre-kink’ trail index to larger values. The general situation with a harder polar ‘jet’ emis-

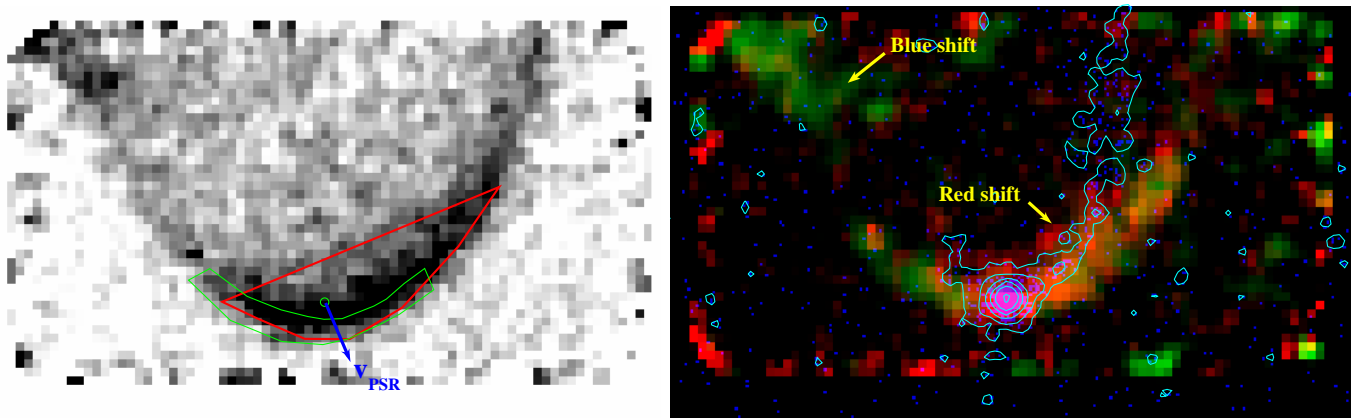


FIG. 2.— Left: KOALA field integrated over the  $H\alpha$  line and background subtracted. The pulsar position and proper motion are indicated, along with the Rangelov et al. (2017) ‘F125LP’ bow shock aperture (green) and our ‘ $H\alpha$  apex’ aperture (red). Right: Apex velocity structure: KOALA maps  $-69$  to  $-37$   $\text{km s}^{-1}$  (green) and  $+48$  to  $+77$   $\text{km s}^{-1}$  (red), with the *CXO* 0.3-3 keV photons in blue, and cyan contours. The X-ray jet corresponds to a red-shifted portion of the  $H\alpha$  shell, a blue-shifted region is seen to the NE.

sion and softer equatorial ‘torus’ emission seems present in many PWNe. A good example is Geminga, where the long outer tails, which similarly bend to follow a bow shock shape while maintaining a hard X-ray spectrum, are interpreted as polar jets (Posselt et al. 2017).

## 2.2. *HST* imaging

Given that the small shock stand-off is poorly resolved in ground-based  $H\alpha$  imaging, we attempted an observation of the  $H\alpha$  limb using the *Hubble Space Telescope* WFC3 camera with the narrow (1.4nm) F656N  $H\alpha$  filter (Program 14364). Two orbits were used on August 14, 2016 with 5209 s exposure in F656N and a 179 s F606W exposures for continuum measurement. Despite careful placement of the nebula apex near the readout node, pre-flashing of the WFC3 and tuned dithered combinations of the long F656N frames, the nebula  $H\alpha$  limb was not detected. We attribute this to the poor WFC3 Charge Transfer Efficiency at the very low count level for this rather faint nebula. This does mean that the  $H\alpha$  limb is substantially resolved, as the count rate per pixel for a nebula limb width  $< 0.3''$  should have allowed a WFC3 detection. Unfortunately the cycle 22 continuum images of Program 13783 (PI Pavlov) were not available while these observations were being planned. These show a relatively bright and red pulsar point source, so that a larger fraction of the orbit devoted to the F606W continuum frame would have given a red detection or useful upper limit. In the end these *HST* exposures served to help reference the ground-based  $H\alpha$  frames to the precise pulsar position as measured in the F125LP and F475X continuum images.

## 2.3. KOALA Spectroscopy

At present the best  $H\alpha$  direct image available is the 600 s SOAR/GHTS W012 image of BR14. We sought to improve this and to gather kinematic information on the forward shock structure by observing with the KOALA integral field unit (IFU) on the AAT under the NOAO time exchange program (Project NOAO/36). KOALA was configured with  $1.25''$  sampling, so that the 1000 fibers covered  $27.4'' \times 50.6''$ , sufficient to measure the PWN apex. The fibers fed the AAOMega spectrograph with the red arm using the 2000R grating covering  $\sim 6273 - 6737\text{\AA}$  at a resolution of  $0.23\text{\AA}/\text{pixel}$  ( $10.5$   $\text{km/s}$  at  $H\alpha$ ). For the blue arm we used the 1500B grating, covering  $\sim 4301 - 5077\text{\AA}$  at  $0.23\text{\AA}/\text{pixel}$  ( $23.5$   $\text{km/s}$  at  $H\beta$ ). Observations were made on October 19-20, 2014 and on July 20,

2015. Seeing was variable, typically  $1.5 - 2.0''$  but occasionally as poor as  $4''$ . Both runs suffered intermittent clouds and instrument problems. Nevertheless we were able to collect  $13 \times 1800$  s on J2124, with the pointing dithered between exposures. Flux calibration exposures of the continuum standards and of the emission lines standards PN 205.8–26.7, PN211.0–03.5, PN253.3–03.9 and BoBn-1 were obtained with the same set-up. Since conditions were not photometric we will have non-statistical uncertainty in the calibrated fluxes; we estimate these at  $\sim 20\%$  by comparing individual exposures.

All data were reduced with the AAT-provided 2dFdr-v6.2 software with KOALA configuration files. Fibers were traced on the flat-field spectra, allowing optimal extractions of the arcs, standards and objects. Wavelength calibrations were established against CuAr arcs while the spectra were flat fielded using a combination of dome flats and twilight flats. Final flat fielding was achieved by monitoring sky lines in the individual exposures. The 2dFdr software combines the dithered exposures into data cubes sampled on a  $0.75''$  grid. These were sky subtracted by defining background regions well away from stars and nebulosity. These regions were chosen to surround the nebula of interest, when possible. Residual flat field errors led to some imperfection in the sky subtraction.

The integrated  $H\alpha$  image (Figure 2, left) shows an improved measurement of the apex surface brightness distribution, although the IFU sampling and seeing substantially smooth the limb. Since no continuum stars appear in the KOALA field, we had to align the image using this blurred  $H\alpha$  limb, referenced through the SOAR  $H\alpha$  image and the *HST* F606W frame. This alignment is uncertain by  $\sim 0.5''$ . J2124 is a relatively slow pulsar and so the velocity spread of the bow shock is only modestly resolved, even for  $H\alpha$ . Nevertheless we do see some interesting features. In the right panel of Figure 2, the redshifted channel shows a ridge of emission inside the limb that follows the X-ray jet. There is also a blue shifted region to the NE that appears to surround the pulsar position 500-600 y in the past and is presently marked by a bulge and brightening at the limb. Deeper velocity channel images with larger-scale coverage (and ideally few  $\text{km/s}$  resolution) would be needed to fully map these structures.

Our data provide an opportunity to check other emission lines and compare with shock models. In Rangelov et al. (2017) a  $52$   $\text{arcsec}^2$  aperture was defined covering the brightest portion of the F125LP UV shock limb. This aperture does

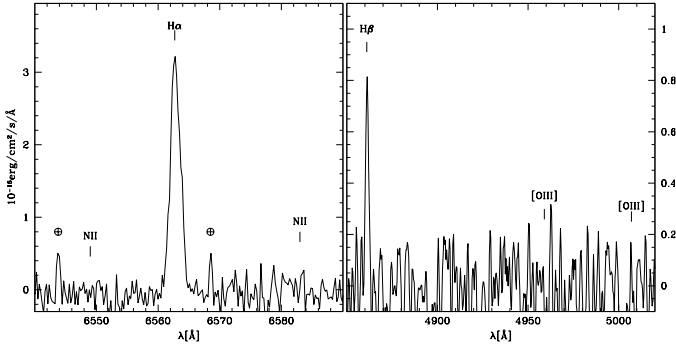


FIG. 3.— Portions of the KOALA IFU spectrum, integrated over the ‘H $\alpha$  apex’ aperture and background subtracted. Only the Balmer lines are well detected.

not correspond well to the H $\alpha$  limb. As confirmed with the SOAR direct frame, portions of the UV flux lie ahead of this limb. Also, the overall shock is distinctly wider to the west of the pulsar line of motion. We will be interested in the swept up ISM and the distribution about this pulsar velocity axis, including the front and back sides. Thus we define a somewhat larger (108 arcsec<sup>2</sup>) aperture covering this ‘H $\alpha$  apex’ and extending 3.5'' behind the pulsar with a base perpendicular to the projected pulsar motion.

Averaging over this aperture we measure the Balmer decrement  $r_{\alpha\beta} = 3.7 \pm 0.4$  with a negligible correction for interstellar extinction (Figure 3). This is in reasonable agreement with the expected ratio  $r_{\alpha\beta} = 3.3$  at  $v \approx 100 \text{ km s}^{-1}$  ( $T \approx 10^5 \text{ K}$ , Raga et al 2015). The forbidden lines associated with radiative cooling are not detected, with upper limits of  $1 \times 10^{-17} \text{ erg cm}^{-2} \text{ s}^{-1}$  for OIII 5007 and  $1 \times 10^{-17} \text{ erg cm}^{-2} \text{ s}^{-1}$  for NII 6582. Rangelov et al. (2017) present some radiative models for the observed UV flux; it is clear that the observed forbidden line/Balmer ratios are much lower than expected for such a model; the bulk of the observed line emission comes from the non-radiative zone of the bow shock.

### 3. PWN/BOW SHOCK STRUCTURE

It is apparent from Figures 1 and 2 that the shock front is very close to the the pulsar along the proper motion axis and, as noted by BR14, the shock is very flat at the apex and asymmetric about this velocity axis. In Vigelius et al. (2007) this asymmetry was primarily ascribed to gradients in the ambient ISM. However, now the ACIS image gives us a clear view of strong asymmetry in the (reverse shocked) pulsar wind. Identifying the trail as a polar jet, as argued above, means that the counter-jet appears at least  $5\times$  fainter. This polar flux is also dramatically brighter than the softer equatorial excess. This suggests a strongly asymmetric momentum distribution, with a dramatic concentration to one side of the spin equator. We have extended standard bow shock modeling to explore this possibility.

In the X-ray the NW jet is strong, and well confined; the SE jet is faint or absent. The softer outflow at PA  $\sim 60^\circ$  which we identify as equatorial is also more prominent on the trailing side. It is natural to ascribe this to the ram pressure of the oncoming ISM. However we now have a good measurement of the pulsar-bow shock standoff distance from the UV and the detailed limb and rough velocity structure of the H $\alpha$  forward shock from the optical. Thus more detailed comparison with shock model geometries is justified.

Wilkin (2000) provides elegant closed form expressions for the shape of the momentum-balance contact discontinuity (CD). For an isotropic wind, the nose of the CD has a char-

acteristic standoff distance in the direction of the  $v_p$  pulsar motion of

$$r_0 = \left( \dot{E} / 4\pi\rho v_p^2 c \right)^{1/2}, \quad (1)$$

where we have assumed a relativistic massless wind ( $\alpha = 0$  in Wilkin’s notation).

The formulae describe the CD shape for an axisymmetric momentum flux  $p(\theta_*) = \dot{E}(\theta_*)/c = \sum_n c_n \cos^n \theta_*$ , with  $\dot{E}(\theta_*)$  the co-latitude dependence of the wind and the spin axis at angle  $\lambda$  to the space velocity with phase angle  $\phi_\lambda$ . See equation (A2) for the relation of these angles to the velocity-aligned system. Wilkin (2000) gives explicit expressions up to  $n = 2$ .

Since the X-rays show the jet to be rather narrow and since the H $\alpha$  apex is asymmetric about  $v_{PSR}$ , we found it helpful to expand further to better match the shock shape. The needed components  $G_{w,\tilde{\omega}}$  and  $G_{w,z}$  of the momentum integral are given to  $n = 4$  in the appendix. With these the shock limb is given as

$$r(\theta, \phi) = r_0 (6G_{w,z} - 6G_{w,\tilde{\omega}} \cot\theta)^{1/2} / \sin\theta \quad (2)$$

and the velocity of well-mixed flow tangent to this limb has amplitude

$$v_t = v_{PSR} [4G_{w,\tilde{\omega}}^2 + (2G_{w,z} - \tilde{r}^2)^2]^{1/2} / \tilde{r}^2 \quad (3)$$

with  $\tilde{r} = (r/r_0)\sin\theta$ .

In the numerical realizations for a given set of  $c_n$ ,  $\lambda$  we compute the CD shape (Eq. 2) referenced to the proper motion axis  $\vec{v}$ . We incline this vector by angle  $i$ , set  $\phi_\lambda$  to orient the mis-aligned spin axis relative to the plane of the sky and then compute the image by shooting rays through this structure, summing the emissivity at each limb intersection and projecting to the plane of the sky. The emissivity prescription is at present a simple scaling to the swept up ISM density at  $r(\theta, \phi)$ . We also take the amplitude of the velocity in Equation 3, compute the tangent vector in the constant  $\phi$  plane at  $r(\theta, \phi)$  and project this velocity along the Earth line-of-sight. The surface flux is assigned to the velocity vector representing this tangent flow (and an additional component in a narrow distribution around zero velocity to represent emission from the collisionally excited neutrals in the shocked ISM) and summed into velocity planes of a data cube. The entire structure is rotated to match the observed  $\vec{v}$  axis and a world coordinate system is assigned to match the pulsar position and image scale. While the intensity distribution is arbitrary and will not match the details of the observed bow shock, the CD shape (and approximate velocity distribution) can be compared with the KOALA data cubes.

We should recall that the observed radiation comes from the forward (Balmer, UV) and reverse (X-ray) shocks. The forward shock stands off from the CD, by a factor estimated as  $\sim 1.3\times$  at the nose of a bow shock with a simple isotropic wind (Aldcroft, Romani & Cordes 1992; Bucciantini 2002). The shock pressure serves also to make the forward shock limb smoother, so it is less sensitive to the fine details of the wind anisotropy. Another difference to the simple model is that some line emission will be prompt, as the neutral ISM particles enter the shocked ISM and experience excitation and charge exchange into excited states. Only after the medium is largely ionized will  $v_t$  fully describe the flow.

The jet asymmetry can be reproduced using  $c_1$  and/or  $c_3$  while the small standoff and jet dominance require large  $c_2$

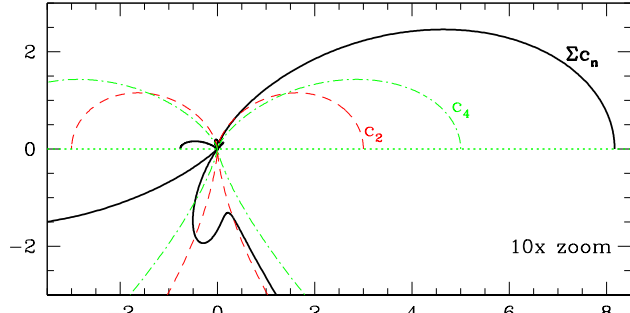


FIG. 4.— Polar plot of PWN momentum distribution for our J2124 model. Symmetric  $\cos^2\theta$  (red) and  $\cos^4\theta$  (green) winds with the same integrated power are shown for comparison. The bottom panel magnifies the arbitrary scale  $10\times$  to show the weak quasi-equatorial component.

and/or  $c_4$ . Our goal is to match the overall shape of the  $H\alpha$  limb, recognizing that the post-shock pressure will make this larger and smoother than the computed CD surface. Any attempt to match the shape with a dominant equatorial flow (large negative  $c_2$ ) and the spin axis aligned with the proper motion fails, given the E-W asymmetry of the limb about the proper motion axis. Indeed, we were not able to make a sufficiently ‘flat’ bow shock even for highly equatorial models viewed edge-on (spin axis in the plane of the sky); their apex curvature was always too large. Adding  $c_4$  terms did not significantly help.

Instead, the most promising solutions invoke polar (jet-dominated) models, with a large  $\vec{\Omega} - \vec{v}$  angle. This accords with our spectral inference that the trail is a polar jet, and additionally allows us to produce E-W asymmetry by using the  $c_1$  and  $c_3$  terms. In our modeling we fix the proper motion at the observed  $203^\circ$  angle, with  $\vec{v}$  inclined by an angle  $i$  to the line of sight. We match the projected spin axis  $\vec{\Omega}$  with the  $PA \approx -60^\circ$  axis of the base of the observed jet. Thus this imposes a constraint on the  $\vec{\Omega} - \vec{v}$  angles  $\lambda$  and  $\phi_\lambda$ . The shape is controlled by the four parameters  $c_1 - c_4$ , and an overall normalization factor, which we report for convenience as  $\theta_0$ , the standoff angle of the isotropic wind with the same total momentum flux. This normalization could also be quoted via  $c_0$  and a rescaling of the other coefficients. This is a total of seven model parameters. Unfortunately, the finite pressure standoff means that we cannot directly fit this CD sum to the shock limb shape. But matching the overall shape is surprisingly constraining and the parameters are fairly well determined in the context of this model. Full MHD simulations will be needed for a detailed match.

We have computed a range of CD models, adjusting the  $c_n$  and angles, while holding the velocity vector fixed at the corrected proper motion direction and the spin axis fixed along the jet base. Figures 4 and 5 show the best match found. This is a model with the pulsar velocity inclined  $i = 120^\circ$  from the line of sight ( $30^\circ$  into the plane of the sky), with the spin axis at  $\lambda = 95^\circ$  to  $\vec{v}$ , directed at  $\phi_\lambda = 10^\circ$ . The momentum coefficients are  $c_1 = -0.3$ ,  $c_2 = -0.2$ ,  $c_3 = 4.0$  and  $c_4 = 4.5$ , and the isotropic equivalent standoff angle is  $\theta_0 = 2.1''$ . Figure 4 shows the polar plot of the momentum distribution, while figure 5 compares directly with the  $H\alpha$  limb. For the left panel of figure 5 we have expanded to  $1.3 \times \theta_0$  to show the shape match to the limb. Note that for these coefficients the momentum flux has a weak near-equatorial (‘torus’) component in Figure 4 at  $\theta \approx 110^\circ$  and a near-null at  $\theta \approx 120^\circ$ . These show up in the contact discontinuity shape as the small bulge near the nose and the edge-brightened indentation just to its

east (Figure 5). While a momentum bulge from the weak torus is physically plausible, the near-null is likely just an artifact of the limited number of  $c_n$ . Neither CD feature is expected to show in the forward shock ( $H\alpha$ ) structure, being smoothed by the shocked ISM pressure. The model’s projected spin axis lies along the CXO jet emission and the momentum for the stronger forward jet into the plane of the sky makes a PWN bulge in that direction. The red-shifted KOALA velocity channels are concentrated along this bulge with smaller excursions for the torus’ momentum into the plane of the sky and for the weak counter-jet (cf. Figure 2, right).

Since we can only match the observed shape, rather than fit, we cannot quote formal errors. However, the model shape departs noticeably from the observed limb shape when we shift the parameters by  $\sigma_i \approx 20^\circ$ ,  $\sigma_\lambda \approx 10^\circ$ ,  $\sigma_{\phi_\lambda} \approx 10^\circ$  (linked to  $\lambda$  to set the projected PA),  $\sigma_{\theta_0} \approx 0.1''$ ,  $\sigma_{c_1} \approx 0.2$ ,  $\sigma_{c_2} \approx 0.1$ ,  $\sigma_{c_3} \approx 0.3$  and  $\sigma_{c_4} \approx 0.2$ . Figure 4 shows that even a  $4^{th}$  order expansion does not produce a jet as collimated as that seen in the ACIS image. For this one needs to go to  $n = 8 - 10$  and a numerical approach will be more productive. This may help to further flatten the shock apex and tune the fine structure of the torus and counter-jet contributions.

#### 4. MODELS AND MASSES

The model in section 3 allows us to estimate the total energy flux of PSR J2124–3358. Because many kinematic parameters are available from the precision pulsar timing, this becomes an important test of the pulsar physics. The basic argument was presented in BR14: with a known efficiency of Balmer photons/HI atom entering the shock, the observed  $H\alpha$  flux plus the bow shock geometry give the upstream neutral density. With a distance and proper motion and a possible correction for ionization fraction, this also gives the incident momentum flux. Balancing this with the PWN flux, including correction for the anisotropy, we obtain the spindown power and, using the timing parameters, the neutron star moment of inertia.

Transverse to the projected pulsar motion the  $H\alpha$  apex aperture extends  $26.6''$  in the sky plane. Our asymmetric shock model indicates extension along the jet axis. The 3-D apex aperture has a nearly elliptical cross section with axes  $26.6'' \times 13''$ . With a space velocity  $\mu_\perp d/\sin i = 127d_{410}(\sin i/0.866)^{-1}\text{km s}^{-1}$  (for the corrected transverse velocity and a distance scaled to 410 pc) the apex zone sweeps out a volume  $1.3 \times 10^{41}d_{410}^3(\sin i/0.866)^{-1}\text{cm}^3\text{s}^{-1}$ . In the KOALA data cube the observed  $H\alpha$  photon rate from this zone is  $2.3 \times 10^{-4}H\alpha \text{ cm}^{-2}\text{s}^{-1}$  while in the direct SOAR image we obtain  $2.9 \times 10^{-4}H\alpha \text{ cm}^{-2}\text{s}^{-1}$ . We will adopt the average,  $f_{H\alpha} = 2.6 \times 10^{-4}H\alpha \text{ cm}^{-2}\text{s}^{-1}$ , although the transparency issues during the KOALA run suggest that this is conservative. This flux corresponds to a nebula apex luminosity of  $5.2 \times 10^{39}d_{410}^2 H\alpha \text{ s}^{-1}$ . If we assume electron-ion equilibration the  $H\alpha$  yield is  $\epsilon_{H\alpha} = 0.6(v/100\text{km s}^{-1})^{-1/2}$  per neutral crossing the shock (Heng & McCray 2007), giving  $9.8 \times 10^{39}d_{410}^{5/2}(\sin i/0.866)^{-1/2}\text{HI/s}$ . This implies an upstream HI density  $n_{HI} = 0.076d_{410}^{-1/2}(\sin i/0.866)^{1/2}\text{cm}^{-3}$ , with a total density  $(1 - x_i)^{-1} \times$  larger, for an ionization fraction  $x_i$ . We will assume electron-ion equilibrium in the following sums, as the disequilibrium  $H\alpha$  efficiency is nearly  $10\times$  smaller at these velocities, leading to very large densities and an unreasonable spindown power.

This  $n_{HI}$  is somewhat unusual. By volume most of the HI is in the Warm Neutral Medium (WNM), which at J2124’s

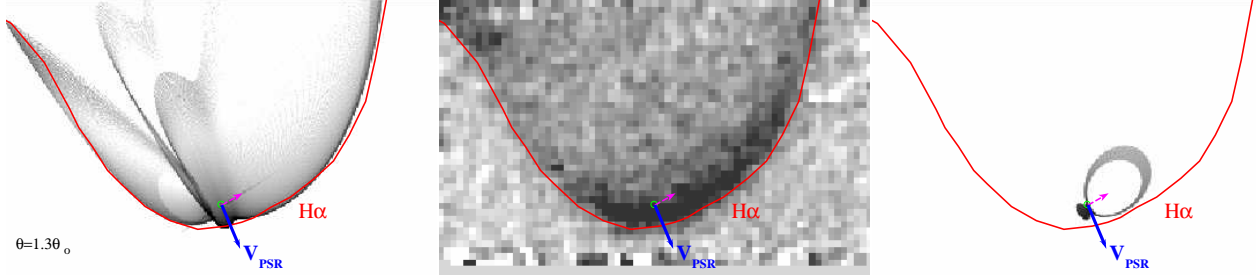


FIG. 5.— PSR J2124–3358 CD model. Left: Direct image of model, with CD scale amplified  $1.3\times$  to show the limb match. Arrows from the pulsar point source show the spin and jet axes. Note that the groove in the model surface is a result of the equatorial component and near-null (see fig 4); such structure is an artifact of the limited number of  $c_n$  used and should not appear in the  $H\alpha$  limb of the pressure-smoothed forward shock. Middle: velocity-integrated KOALA image, with the pulsar velocity and X-ray jet axes indicated. Right: a red-shifted model channel showing  $+55 - 65\text{km s}^{-1}$  emission. The data have a similar, but narrower, red extension along the jet PA (Figure 2). The  $H\alpha$  limb is shown in red in the three panels, for comparison.

290 pc height above the plane has a typical density  $n_{WNM} \approx 0.25\text{ cm}^{-3}$  and is largely neutral with  $x_i \approx 0.05$ . This would produce  $n_{HI}$  and nebular  $H\alpha$  flux  $\sim 3\times$  larger than observed. The Warm Ionized Medium (WIM), in pressure equilibrium at  $n_{WIM} \approx 0.125\text{ cm}^{-3}$  and  $x_i \approx 0.95$ , has a much lower HI density and is not a viable alternative. So we infer that the local medium is partly ionized and has a proton density larger than that of the observed HI. If the ionization is general, preserving pressure equilibrium with the WNM/WIM, the observed  $n_{HI}$  implies  $x_i = 0.55$ . If the ionization is local so that the upstream medium can be over-pressured, the typical  $n_{WNM} \approx 0.25\text{ cm}^{-3}$  density gives  $x_i = 0.70$ .

Our model determines the isotropic equivalent standoff angle as  $2.1''$ , i.e.  $r_0 = 1.29 \times 10^{16} d_{410}\text{cm}$ . Thus from equation (1) we write

$$\dot{E} = 4\pi^2 I \dot{P} / P^3 = 4\pi\rho v^2 cr^2. \quad (4)$$

The observed flux  $f_{H\alpha}$  gives us our estimate of  $n_{HI}$  which we convert to mass density as  $\rho = \mu m_p n_{HI} / (1 - x_i)$  for mean mass per particle  $\mu m_p$ . Plugging in gives  $\dot{E} = 1.77 \times 10^{33} d_{410}^{7/2} (\sin i / 0.866)^{-3/2} (1 - x_i)^{-1} \text{erg s}^{-1}$ . Applying the Shklovskii correction (Shklovskii 1970), this gives us the neutron star moment of inertia as

$$I = \dot{E} P^3 / [4\pi^2 (\dot{P}_{obs} - v_{\perp}^2 P / dc)] \quad (5)$$

For J2124 we have  $P = 4.93\text{ms}$ ,  $\dot{P}_{obs} = 2.057 \times 10^{-20}$  (Shklovskii-corrected  $\dot{P} = 7.27 \times 10^{-21}$ ), giving

$$I_{45} = 0.74 d_{410}^{7/2} (\sin i / 0.866)^{-3/2} (1 - x_i)^{-1} \quad (6)$$

in standard units of  $10^{45}\text{g cm}^2$ . From the ionization discussion above we see that this is  $I_{45} = 1.66$  for ionization maintaining WNM pressure equilibrium ( $x_i = 0.55$ ) and  $I_{45} = 2.43$  if we partly ionize the typical WNM density ( $x_i = 0.70$ ).

We would like to relate this moment of inertia to the neutron star mass. Given the existence of  $2M_{\odot}$  neutron stars, the equation of state is fairly stiff and from Lattimer & Schutz (2005) we see that

$$I_{45} \approx [0.8 - 1.2] (M/M_{\odot})^{3/2}, \quad (7)$$

where the prefactor  $[\ ]$  covers the range of acceptable EOS from relatively soft to very stiff. This can be used to make a neutron star mass estimate

$$M_{NS} = [0.73 - 0.95] \left( \frac{f_{H\alpha}}{2.6 \times 10^{-4} \text{cm}^2 \text{s}^{-1}} \right)^{2/3} (1 - x_i)^{-2/3} d_{410}^{7/3} (\sin i / 0.866)^{-1} M_{\odot}. \quad (8)$$

This estimate again supports our inference of substantial ionization of the ambient WNM, but highlights the uncertainty introduced by this factor. For  $x_i = 0.55$  the allowed range is  $1.24 - 1.63M_{\odot}$ , allowing but not demanding substantial accretion during spin-up. For  $x_i = 0.70$  we infer  $1.60 - 2.10M_{\odot}$ , so that significant mass growth is required. However, even then uncertainty in the other parameters precludes strong conclusions. In particular while the present parallax error is only  $-17\%/+22\%$ , the strong distance dependence leads to a  $-35\%/+59\%$  uncertainty in the neutron star mass. Systematic (model) uncertainties are at present smaller; the crucial factors are the nebula cross section and pulsar velocity inclination, which are constrained by the direct imaging. In the context of the model matches, our ‘chi-by-eye’ approach shows a  $\sim 10\%$  range in  $I_{45}$ , varying these geometric terms over the range of acceptable fits. We consider this a ‘systematic’ error range for this model – of course if the model is incorrect the true  $I_{45}$  could differ by more. Uncertainty in the measured  $f_{H\alpha}$  contributes  $\sim 20\%$  to  $I_{45}$  or  $\sim 13\%$  to  $M_{NS}$ .

## 5. CONCLUSIONS

We measure strong asymmetry in PSR J2124–3358’s bow-shock and PWN. In the ACIS X-ray data, the reverse shock emission seems to be dominated by a polar jet trailing the pulsar motion. There are a few photons plausibly assigned to counter-jet emission, but comparing similar areas in the few arcsec at the base of the jets (before the bow shock) the counter-jet is at least  $5\times$  fainter. There is also a weak equatorial outflow, with a softer spectrum. Both polar and equatorial emission appear swept back by the pulsar motion and bounded by the UV/ $H\alpha$  PWN.

The *HST*-detected UV bow shock lies near the forward edge of the observed  $H\alpha$  emission. This adds credence to the idea that the observed F125LP flux arises in the shocked ISM. However, our KOALA IFU spectroscopy of the bow shock apex shows that the cooling lines from such shocked emission do not dominate the nebula. For example, Rangelov et al. (2017) Figure 9 shows  $\text{OIII } 5007/H\beta \approx 1$  for the thermal emission from a cooling plane shock; our upper limit is  $5007/H\beta < 0.06$ . Also from Figure 6 of Rangelov et al. (2016) we infer a predicted thermal plane shock  $H\alpha$  flux of  $\sim 3.3 \times 10^7 \text{H}\alpha \text{ cm}^{-2} \text{s}^{-1}$  at the source or  $2.8 \times 10^{41} \text{H}\alpha \text{ s}^{-1}$  for our full apex zone. Our observed flux for this bow shock zone is only 2% of this value (of which only  $\sim 5\%$  can be thermal emission). Clearly radiative emission can only play a small role in the bow shock, where the shocked gas is advected far down stream before it cools. This explains the extreme Balmer dominance and indicates that we should also attribute the UV emission to a non-thermal model, in which

PWN  $e^\pm$  infiltrate the shocked ISM and radiate. We know of no detailed model for this case, but multi-band continuum imaging of the shock should be able to distinguish the synchrotron emission from the thermal scenario.

The KOALA data also provide an improved S/N map of the nebula limb (albeit at low spatial resolution) and information on the velocity-dependent morphology. Upgrading the analytic bow shock models to allow narrower polar outflows, we have attempted to match the KOALA shape and velocity dependence, while holding the pulsar transverse velocity vector and the projected spin (jet) axis vector fixed. The result indicates a pulsar moving  $\sim 30^\circ$  into the plane of the sky with an approximately orthogonal spin axis. The very large jet/counter-jet asymmetry (a factor of  $\sim 10$  for the integrated flux in our model) induces an E-W asymmetry about the proper motion axis and makes the bowshock ovoid in its cross section.

The origin of this asymmetry is unclear. Images of other PWNe with apparent polar jets do show asymmetries, but these are generally smaller (e.g. Kargaltsev et al. 2017). At the base of such jets unequal fluxes can be attributed to Doppler beaming but on larger scales sweepback is the likely culprit. In J2124 we might have attributed the dimness of the counter-jet to ram pressure suppression or sweepback, but we have the evidence of the H $\alpha$ /UV forward shock shape to show that the standoff (and hence the outflow/ram pressure ratio) is smaller on that side of the spin axis. Hence we infer a true momentum asymmetry. Modest momentum asymmetries have long been inferred when the pulsar has an off-center dipole field, the ‘Harrison-Tademaru’ effect (see Lai, Chernoff & Cordes 2001). For a simple vacuum dipole, the momentum asymmetry is, however,  $< 2\times$ ; we can only speculate that a more complex multipole configuration or plasma effects might increase the allowed asymmetry.

In the context of this asymmetric model, the observed H $\alpha$  flux and nebula geometry give an estimate of the PWN momentum flux needed to balance the oncoming ISM. This momentum flux gives the spindown power and via the pulsar timing parameters an estimate of the moment of inertia. These estimates depend on the upstream ionization, which we estimate as  $x_i = 0.55 - 0.70$ . The PWN itself may provide a source of such ionization. We checked if the UV flux (dominated by the bow shock) itself could photoionize the upstream WNM. The observed  $L_{6.2\text{eV}-9.9\text{eV}} = 1.9 \times 10^{29} \text{erg s}^{-1}$  (Rangelov et al. 2017) provides an H-ionizing cross-section flux of  $a\dot{N}_i = \int dN/d\epsilon a_H(\epsilon) d\epsilon \approx 4 \times 10^{22} \text{cm}^2 \text{s}^{-1}$  (for an assumed flat spectrum), which only ionizes over a characteristic distance  $r_i = a\dot{N}_i/4\pi v$  (van Kerkwijk & Kulkarni 2001) or  $\theta_i \approx 0.04''$  for the J2124 distance and parameters. Since the bow shock is detected in neither the X-ray nor the optical, the index and flux cannot be very different than assumed here; with  $\theta_i \ll$  the standoff angle  $\theta_0$ , the UV cannot strongly pre-ionize the ambient medium.

However the UV-emitting electrons themselves are a possible source of cosmic rays to pre-ionize the medium. We already infer that the PWN  $e^\pm$  can cross the CD to generate UV emission in the forward bow shock. Since the pulsar spindown power goes mostly into  $e^\pm$  the energy density at offset  $\theta$  is  $\sim \dot{E}/(4\pi d^2 \theta^2 c) \approx 100/\theta_{\text{arcsec}}^2 \text{eV cm}^{-3}$ , so if a few percent of the PWN power escapes it can dominate the local ionizing cosmic ray density. Such escape may be particularly enhanced for J2124 because of the PWN anisotropy

and the small standoff at the apex. Recall that the Eastern (E) section of the shock apex, where the counter-jet impacts and the UV flux (and hence ISM penetration of PWN  $e^\pm$ ) is largest, also shows fainter H $\alpha$  emission (Figure 2). One can speculate that this is partly due to greater pre-ionization in this portion of the bow shock. However one should also note that the faintest portion of the E limb is nearly parallel to the proper motion: very little fresh HI enters the shock in this region in any event. One might further speculate that if, contrary to expectation, very little ionization occurs in the bow-shocked ISM (Morlino, Lyutikov & Vorster 2015), then the effective (ionized) ISM density might be much larger in the E half of J2124’s bow shock than in the west. Such non-uniform ionization (traceable to the PWN outflow geometry) might then contribute to the asymmetry of the H $\alpha$  limb. We do not pursue this further here, although it is a fruitful scenario for additional study.

The WNM ionization, while almost certainly present, is thus poorly understood. In turn this leads to uncertainty in the J2124 mass and moment of inertia. Accordingly bow shocks in lightly ionized  $x_i \approx 0$  WNM will provide the most robust evidence for large  $I_{45}$  and  $M_{NS}$  since the ionization correction is small. This appears not to be the case for J2124. If we can observationally constrain the upstream temperature and ionization state this would help reduce the uncertainty. One approach would be to obtain high resolution spectra measuring the narrow (collisional excitation) line component in the non-radiative shock, whose width is sensitive to the upstream pre-ionization and heating. This component is not detected in our moderate resolution spectra. However at present other factors, principally the distance uncertainty, dominate the  $I_{45}$  error budget, so better distances and H $\alpha$  flux measurements are needed before ionization and model uncertainties are the limiting factor.

We are left with an interesting, but rather imprecise result. With our best estimate of the state of the upstream medium (WNM with preshock ionization) we infer  $M_{NS} = 1.60 - 2.10 M_\odot$  (depending on EOS choice), which implies substantial mass accretion during the recycling. If the pre-ionization only produces pressure equilibrium our measured  $n_{HI}$  leads to an estimate  $M_{NS} = 1.24 - 1.63 M_\odot$ , so softer allowed equations of state imply mass growth during recycling, while stiffer EOS do not require it. Of course, with a combined error as large as 50%, dominated at present by the parallax uncertainty, none of these conclusions are very robust. Still, we have used our PWN measurements to gain some insights into the neutron star spin orientation and some spindown power constraints. It will be particularly interesting to compare the results of our modeling with measurements of spin orientation and  $M/R$  constraints from the new NICER mission where PSR J2124–3358 is one of the 3-4 prime early targets (Oezel et al. 2016). Indeed, if NICER succeeds in making a radius measurement for this pulsar then our  $I$  estimate will be particularly interesting, since no orbital mass measurement is available and only light bending constraints are expected.

We thank Newton C.-S. Cheng for assistance with reduction of the KOALA data cube and the anonymous referee whose careful reading caught a number of typographical errors in the equations and whose comments led to improvement of the text. This work was supported in part by NASA grants GO6-17059X (CfA) and GO-14364 (STScI).

## REFERENCES

- Aldcroft, T. L., Romani, R. W. & Cordes, J. M. 1992, *ApJ*, 400, 638  
 Bisnovatyi-Kogan, G. S. & Komberg, B. V., *Astron. Zh.*, 51, 373 [Engl. transl. *Sov. Astron.* 18 (1975) 2171.]  
 Brownsberger, S. & Romani, R. W. 2014, *ApJ*, 784, 154  
 Bucciantini, N. 2002, *AA*, 387, 1066  
 Gaensler, B. M., Jones, D. H. & Stappers, B. W. 2002, *ApJ*, 580, L137.  
 Heng, C. Y. & McCray, R. 2007, *ApJ*, 654, 923  
 Hui, C. Y. & Becker, W. 2006, *AA*, 448, L13  
 Johnson, D. H. R. & Soderblom, D. R. 1987, *AJ*, 93, 864  
 Kargaltsev, O., Pavlov, G. G., Klinger, N. & Rangalev, B. 2017, *J. Plasma Phys.*; arXiv170800456  
 Lai, D., Chernoff, D. F. & Cordes, J. M. 2001, *ApJ*, 549, 1111  
 Lattimer, J. M. & Schutz, B. F. 2005, *ApJ*, 629, 979  
 Morlino, G., Lyutikov, M. & Vorster, M. 2015, *MNRAS*, 454, 3886  
 Oezel, F., Psaltis, D., Arzoumanian, Z., Morsink, S. & Bauboeck, M. 2016, *ApJ*, 832, 92  
 Posselt, B., Pavlov, G. G., Slane, P. O., Romani, R. W., Bucciantini, N. et al 2017, *ApJ* 835, 66  
 Raga, A. C., Reipurth, B., Castellanos-Ramirez, A., Chiang, H.-F. & Bally, J. 2015, *ApJ*, 798, L1  
 Rangelov, B., Pavlov, G. G., Kargaltsev, O. et al. 2016, *ApJ*, 831, 129  
 Rangelov, B., Pavlov, G. G., Kargaltsev, O., et al. 2017, *ApJ*, 835, 264  
 Reardon, D. J., Hobbs, G., Coles, W. et al. 2016, *MNRAS*, 455, 1751  
 Ruderman, M., Shaham, J. & Tavani, M. 1989, *ApJ*, 336, 507  
 Shklovski, I. S. 1970, *Sov. Astron.*, 13, 562  
 Smarr, L. L. & Blandford, R. D. 1976, *ApJ*, 207, 574  
 van Kerkwijk, M. H. & Kulkarni, S. R. 2001, *AA*, 380, 221  
 Vigelius, M., Melatos, A., Chatterjee, S., Gaensler, B. M. & Ghavamian, P. 2007, *MNRAS*, 374, 793  
 Wilms, J., Allen, A. & McCray, R. 2000, *ApJ*, 542, 914  
 Wilkin, F. P. 2000, *ApJ*, 532, 400  
 Zavlin, V. E. 2006, *ApJ*, 638, 951

## APPENDIX

## BOW SHOCK MOMENTUM FUNCTIONS

For the convenience of others wishing to simulate asymmetric thin bow shocks, we provide a further expansion of the momentum integrals in Wilkin (2000). These expressions assume an axisymmetric relativistic massless pulsar wind (Wilkin's  $\alpha = 0$ ) with momentum distribution

$$p(\theta_*) = \sum_n c_n \cos^n \theta_* \quad (\text{A1})$$

with  $\theta_*$  the co-latitude to the pulsar spin axis. The relationship between the spin- ( $\theta_*$ ,  $\phi_*$ ) and velocity- ( $\theta$ ,  $\phi$ ) referenced coordinate systems is

$$\begin{aligned} \sin \theta_* \cos \phi_* &= \sin \theta \cos \phi \\ \sin \theta_* \sin \phi_* &= \sin \theta \sin \phi \cos \lambda - \cos \theta \sin \phi \\ \cos \theta_* &= \sin \theta \sin \phi \sin \lambda - \cos \theta \cos \phi \end{aligned} \quad (\text{A2})$$

where, following Wilkin's notation the pulsar spin axis is oriented at angle  $\lambda$  to the pulsar velocity vector with orientation angle  $\phi_\lambda$ ;  $\phi_\lambda = 0$  places the spin axis in the plane of the sky.

In writing the  $G$  integrals we define  $p = \sin \phi \sin \lambda$  and  $q = \cos \lambda$  for convenience. We will carry out the expansion to  $n = 4$  so the normalization condition is  $c_0 = 1 - c_2/3 - c_4/5$ . Thus  $c_{2,4}$  determine the equatorial concentration, while  $c_{1,3}$  determine the polar asymmetry. Then at angle  $\theta$  to  $\vec{v}_{PSR}$  the parallel component is

$$\begin{aligned} G_{w,\omega} &= (c_0/2) [\theta - \cos \theta \sin \theta] + \\ & (c_1/3) [4p(2 + \cos \theta) \sin^4(\theta/2) + q \sin^3 \theta] + \\ & (c_2/32) [q^2(4\theta - \sin 4\theta) + p^2(12\theta - 8\sin 2\theta + \sin 4\theta) + 16pq \sin^4 \theta] + \\ & (c_3/30) [3pq^2(4 + \cos^3 \theta [3\cos 2\theta - 7]) + 8p^3(19 + 18\cos \theta + 3\cos 2\theta) \sin^6[\theta/2] + q^3(7 + 3\cos 2\theta) \sin^3 \theta + 18p^2q \sin^5 \theta] + \\ & (c_4/192) [64pq^3(2 + \cos 2\theta) \sin^4 \theta + 128p^3q \sin^6 \theta + q^4(12\theta + 3\sin 2\theta - 3\sin 4\theta - \sin 6\theta) + \\ & p^4(60\theta - 45\sin 2\theta + 9\sin 4\theta - \sin 6\theta) + 6p^2q^2(12\theta - 3\sin 2\theta - 3\sin 4\theta + \sin 6\theta)]. \end{aligned} \quad (\text{A3})$$

The component perpendicular to the velocity is

$$\begin{aligned} G_{w,z} &= (c_0/2) [\sin^2 \theta] + \\ & (c_1/3) [q(1 - \cos^3 \theta) + p \sin^3 \theta] + \\ & (c_2/16) [4q^2(1 - \cos^4 \theta) + 4p^2 \sin^4 \theta + pq(4\theta - \sin 4\theta)] + \\ & (c_3/10) [2q^3(1 - \cos^5 \theta) + p^2q(4 + \cos^3 \theta [3\cos 2\theta - 7]) + pq^2(7 + 3\cos 2\theta) \sin^3 \theta + 2p^3 \sin^5 \theta] + \\ & (c_4/48) [8q^4(1 - \cos^6 \theta) + 24p^2q^2(2 + \cos 2\theta) \sin^4 \theta + 8p^4 \sin^6 \theta + pq^3(12\theta + 3\sin 2\theta - 3\sin 4\theta - \sin 6\theta) + \\ & p^3q(12\theta - 3\sin 2\theta - 3\sin 4\theta + \sin 6\theta)]. \end{aligned} \quad (\text{A4})$$